Crystal Structure of Human Protein Tyrosine Phosphatase 1B

David Barford,* Andrew J. Flint, Nicholas K. Tonks

Protein tyrosine phosphatases (PTPs) constitute a family of receptor-like and cytoplasmic signal transducing enzymes that catalyze the dephosphorylation of phosphotyrosine residues and are characterized by homologous catalytic domains. The crystal structure of a representative member of this family, the 37-kilodalton form (residues 1 to 321) of PTP1B, has been determined at 2.8 Å resolution. The enzyme consists of a single domain with the catalytic site located at the base of a shallow cleft. The phosphate recognition site is created from a loop that is located at the amino-terminus of an α helix. This site is formed from an 11-residue sequence motif that is diagnostic of PTPs and the dual specificity phosphatases, and that contains the catalytically essential cysteine and arginine residues. The position of the invariant cysteine residue within the phosphate binding site is consistent with its role as a nucleophile in the catalytic reaction. The structure of PTP1B should serve as a model for other members of the PTP family and as a framework for understanding the mechanism of tyrosine dephosphorylation.

The phosphorylation of tyrosine residues is an essential element of many signal transduction pathways triggered by hormones, mitogens, and oncogenes that lead to processes such as cell growth, proliferation, and differentiation (*1*). Protein phosphorylation is reversible and controlled by the opposing action of protein kinases and phosphatases that catalyze phosphorylation and dephosphorylation, respectively. The role of protein tyrosine kinases (PTKs) in promoting signaling responses has been well documented. However, the complexity of structure, function, and mode of regulation of protein tyrosine phosphatases (PTPs), as well as possible mechanisms by which PTPs and PTKs cooperate to control cellular phosphotyrosine levels, has only recently been appreciated (*2–4*).

The PTPs are a large (>40 members) and diverse family of proteins present in all eukaryotes (*2–4*). Each PTP is composed of at least one conserved domain characterized by an 11-residue sequence motif (I/V)HCXAGXXR(S/T)G containing the cysteine and arginine residues known to be essential for catalytic activity (*5–8*). The sequences of PTPs share no similarity to serine or threonine, acid, or alkaline phosphatases (*2*). The diversity in structure within the PTP family results primarily from the variety of noncatalytic sequences attached to the NH_2- or COOH-termini of the catalytic domain. As with PTKs, receptor-like transmembrane PTPs are known, suggesting a potential to control signaling events through ligand-modulated dephosphorylation of phosphotyrosine proteins. Receptor-like PTPs have amino-terminal extracellular segments and most have two tandemly repeated intracellular phosphatase domains. The diversity of the extracellular segments presumably reflects the variety of ligands to which they may respond. The extracellular segments of one class of receptor PTPs are related to adhesion molecules of the immunoglobulin superfamily, which for one member, PTPμ, mediates homophilic binding interactions, perhaps linking cell-cell interactions with control of PTP activity (*9*). Cytosolic PTPs have a single catalytic domain flanked by targeting and regulatory sequences including SH2 domains, which recognize phosphotyrosine residues within sequence-specific contexts (*10–15*), and band 4.1 domains, which suggest targeting to interfaces between the plasma membrane and the cytoskeleton (*16, 17*), and domains homologous to lipid-binding proteins (*18*). The presence of such motifs indicates an important role for subcellular compartmentalization in the control of PTP activity.

The recently discovered dual specificity phosphatases p80cdc25 (*19*) and MKP-1 (MAP kinase phosphatase–1) (*20, 21*), display a highly restricted substrate specificity. These enzymes share the signature motif that characterizes the PTPs, but otherwise display little similarity to the phosphotyrosine-specific enzymes. The PTPs are also present in prokaryotes and viruses, including the dual specificity enzymes Iphp present in the cyanobacterium *Nostoc commune* (*22*) and VH1, which is present in vaccinia virus (*23*). In the pathogenic bacterium *Yersinia*, the causative agent of the bubonic plague, the tyrosine-specific PTP, Yop2b, is an essential virulence determinant (*24*).

Numerous studies have demonstrated the importance of PTPs in physiological processes. Inactivating mutations in an SH2 domain containing PTP (HCP) is the basis for the severe immune dysfunction characteristic of the *motheaten* phenotype in mice (*25, 26*). This phenotype includes multiple defects in the function of T cells, B cells, and granulocytes and, in particular, hyperproliferation of macrophages. These defects suggest that HCP normally functions in the negative regulation of a variety of PTK-induced hematopoietic cell signaling pathways. PTPs have also been implicated as the products of tumor suppressor genes. For example, the gene for receptor-PTPγ is located on human chromosome 3p21, a region frequently deleted in renal and lung carcinomas (*27*). Although these functions point to a negative effect of PTPs

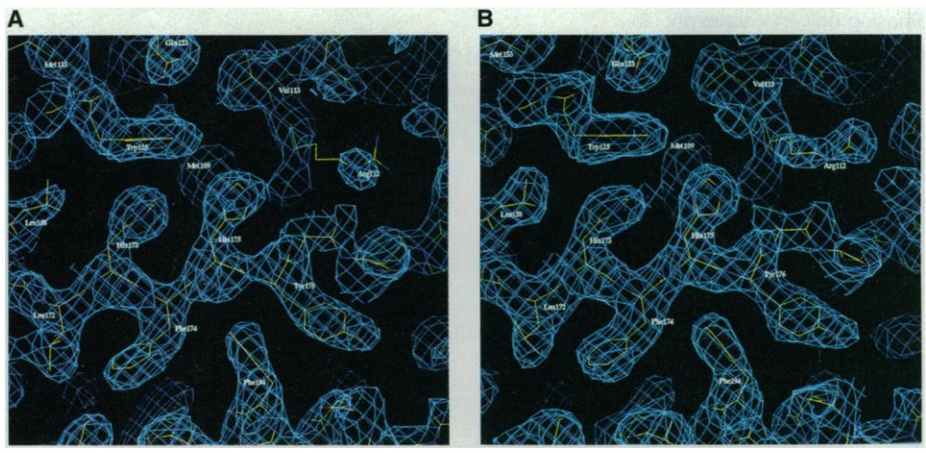

Fig. 1. Portions of the electron density maps superimposed onto the refined atomic coordinates. The maps are contoured at 1.0 σ. (**A**) SIRAS electron density map after solvent flattening for the native PTP1B structure. (**B**) $2F_o - F_c$ electron density map for the PTP1B-tungstate complex. Coefficients used were: $2F_o$(tungstate) − F_c(tungstate) with calculated phases from the refined PTP1B-tungstate coordinates. Displayed with use of O (*45*).

D. Barford is at the W. M. Keck Structural Biology Laboratory, Cold Spring Harbor Laboratory, and A. J. Flint and N. K. Tonks are at Cold Spring Harbor Laboratory, Cold Spring Harbor, NY 11724, USA.

*To whom correspondence should be addressed.

Table 1. Crystal structure determination parameters and results. The crystals were grown at 4°C in a buffer containing 0.1 M Hepes, 0.2 M magnesium acetate (pH 7.5) with 14 percent (w/v) polyethylene glycol (MW, 8000) with the protein at 10 mg/ml (*66a*). The crystals (0.8 by 0.15 by 0.15 mm) were incubated in the same buffer with 25 percent (v/v) glycerol for 40 minutes before being frozen at 100 K (Oxford Cryostream cooling device). The tungstate derivative crystals were prepared by soaking native crystals in crystallization buffer with 5 mM sodium tungstate for 2 hours before they were frozen in liquid nitrogen. Data were collected at beamline X8C at the National Synchrotron Light Source at Brookhaven National Laboratory on the "blue" charge-coupled device detector mounted on a Huber 4 circle goniometer (*43*). The storage ring was operated at 2.5 GeV with a current ranging from 200 to 110 mA. The x-ray wavelength was 1.04 Å and the crystals were maintained in a stream of nitrogen gas at 100 K throughout the experiment. Data were collected and processed with MADNES (*44*) and reflections profile fit with PROCOR (*67*). Integrated reflections were scaled and reduced with FSCALE (*68*). The program PHASES (*69*) was used for data analysis, phase determination, and map calculations. Single isomorphous replacement anomalous scattering (SIRAS) phases determined from the native and tungstate derivative data sets were used to calculate an electron density map at 2.8 Å resolution. The protein phases were improved by solvent flattening the electron density map (*70*) (solvent fraction of 0.62) and further heavy atom refinement against the protein phases calculated from the solvent-flattened SIRAS electron density map. The partial model was refined with the use of the simulated annealing procedure of X-PLOR (*71*) and calculated phases obtained from the refined structure were combined with the original (that is, not solvent-flattened) SIRAS phases and used to determine a new electron density map. The model was rebuilt where necessary and a number of missing residues were built into the electron density map. This procedure was repeated four times, until the *R* factor converged and all the electron density was accounted for. During the latter stages, maps calculated with coefficients $2F_o - F_c$ and $F_o - F_c$ and calculated phases were also inspected. The tungstate derivative data set was used to refine the PTP1B-tungstate ion complex. Data between 6 and 2.85 Å were used in the refinement with Friedel pairs treated separately. No water molecules were included in the refinement.

Crystal parameters

Crystal	Space group	Unit cell parameters a (Å)	b (Å)	c (Å)	α (°)	β (°)	γ (°)	Z
Native	$P3_121$	88.3	88.3	104.0	90.0	90.0	120.0	1
Tungstate	$P3_121$	88.2	88.2	103.9	90.0	90.0	120.0	1

Data collection and processing statistics

Data set	Resolution (Å)	Crystals (*N*)	Measurements (*N*)	Unique reflections Total (*N*)	Unique reflections Complete (%)	Friedel pairs complete (%)	R_{sym}*‖
Native	35–2.85	1	76 241	10 694	98.7	—	0.042
Tungstate	35–2.85	1	48 567	10 098	93.2	93.0	0.044

Phasing statistics

Mean fractional isomorphous difference (tungstate-native)	0.18
Mean fractional anomalous difference (tungstate)	0.05
Resolution range (Å)	35 to 2.85
Tungstate sites (*N*)	1
Mean figure of merit	0.71
Phasing power§ (isomorphous)	2.2
Phasing power§ (anomalous)	2.8
R_{Cullis}†	0.60

Refinement statistics

Crystal structure	Native	Tungstate
Resolution range (Å)	6.0–2.85	6.0–2.85
R factor‡	0.208	0.197
Number of reflections ($F > 0$) (% complete)	9495 (99.0)	16069 (93.1)
Number of protein atoms	2268	2268
Number of tungstate atoms	—	5
Deviation from ideality (rms):§		
Bond lengths (Å)	0.015	0.016
Bond angles (°)	2.2	2.2
Dihedrals (°)	24.7	25.0
Improper (°)	1.82	1.77

*$R_{sym} = \Sigma_h\Sigma_i|I(h) - I_i(h)|/\Sigma_h\Sigma_i I_i(h)$ where $I_i(h)$ and I(h) are the *ith* and mean measurements of the intensity of reflection h. †$R_{Cullis} = \Sigma_h/||F_{PH} - F_P| - F_H|/\Sigma_h|F_{PH} - F_P|$ for centric data, where F_{PH} and F_P are the observed structure factor amplitudes for the tungstate and native data sets of reflection *h*, respectively. F_H is the calculated heavy atom structure factor amplitude of reflection *h*. ‡*R* factor = $\Sigma_h|F_o - F_c|/\Sigma_h F_o$ where F_o and F_c are the observed and calculated structure factor amplitudes of reflection *h*. §Phasing power = root mean square ($<F_H>/E$) where F_H is the heavy atom structure factor amplitude and E is the residual lack of closure error. ‖The mean I/σ for native data is 76.2 and for tungstate data is 55.8.

on PTK-induced signaling events, PTPs may also act positively to trigger such responses. Thus the receptor PTP CD45, through its capacity to dephosphorylate and activate the Src family of PTKs, is essential for initiating downstream signaling responses to stimulation of T and B cell receptors (*28–30*). Furthermore, in *Drosophila*, the cytoplasmic PTP *corkscrew* acts positively in transducing the signal from the receptor PTK, *torso* (*15*).

PTP1B was the first PTP to be isolated in homogeneous form and serves as a model to illustrate several of the properties of PTPs. The enzyme has been purified from human placenta as a protein of 321 amino acids (*31–33*) although the cDNA indicates that this is the NH_2-terminal portion derived from a full-length molecule of 435 residues (*34–36*). The conserved PTP domain is contained within residues 30 to 278, and the COOH-terminal noncatalytic extension serves a regulatory function. The COOH-terminal 35 residues target the enzyme to the cytoplasmic face of membranes of the endoplasmic reticulum (*37*), whereas the preceding 122 residues are predominantly hydrophilic and contain sites for serine phosphorylation. This segment of PTP1B is phosphorylated in vivo and the pattern of phosphorylation is altered in a cell cycle–dependent manner (*38*). PTP1B has been linked to a number of cellular processes. Overexpression of PTP1B antagonizes the action of oncogenic PTKs such as Src (*39*) and Neu (*40*). Potential links to the control of insulin action have also been suggested (*41*). Moreover, a truncated form of PTP1B, in which the regulatory COOH-terminal segment has been removed leaving an active catalytic domain no longer restricted in its intracellular localization, has been implicated in the platelet aggregation response (*42*).

In order to understand more fully the mechanism of action of PTPs we have determined the crystal structure of the 321 residue form of human PTP1B. The enzyme was expressed in *Escherichia coli* in a stable and soluble form whose activity is indistinguishable from that purified from human placenta. The structure described below provides (i) a basis for understanding the specificity of phosphotyrosine recognition and the mechanism of catalysis and (ii) a framework for understanding other members of the protein tyrosine phosphatase family, including the receptor-like forms such as CD45 and the more distantly related dual specificity enzymes such as cdc25. The structure should be useful in the design of novel therapeutic agents to inhibit specific PTPs.

Structure determination. The structure was determined by single isomorphous replacement and anomalous scattering meth-

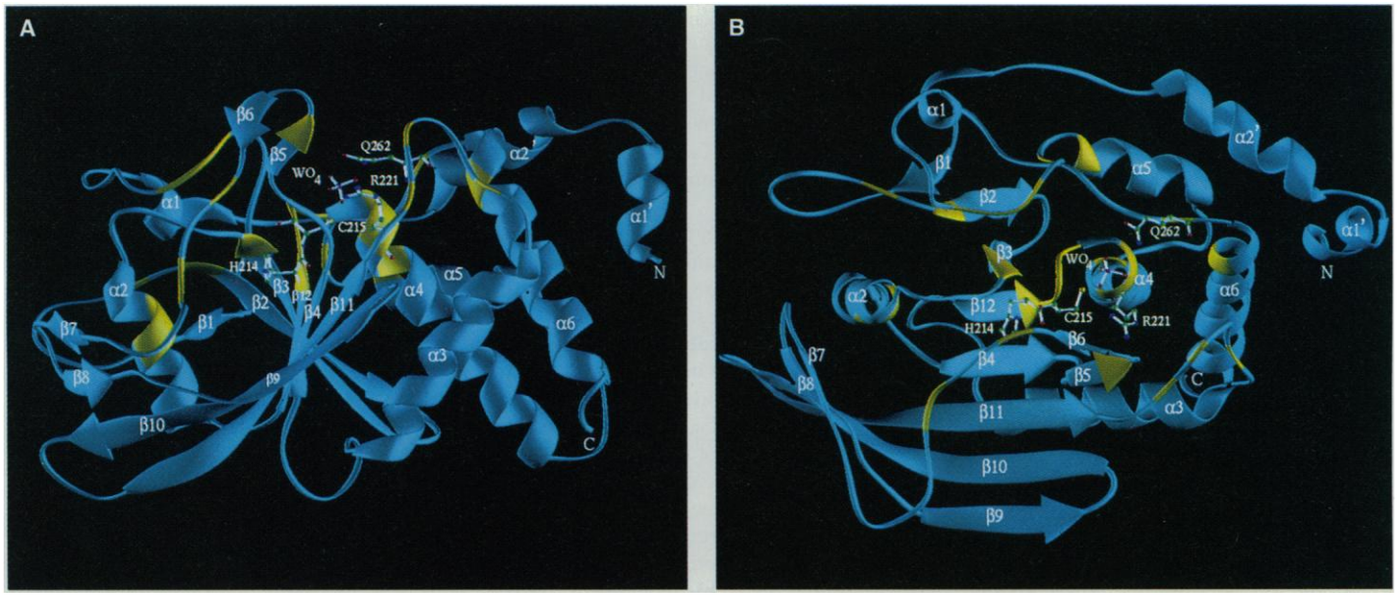

Fig. 2. Views of a ribbon representation indicating the secondary structure elements of PTP1B, the catalytic site, and invariant residues (yellow). The α helices and β strands are labeled. The tungstate ion and the side chains of His^{214}, Cys^{215}, Arg^{221}, and Gln^{262} are shown. (**A**) Viewed onto the edge of the 10-strand β sheet. The catalytic site is located at the COOH-terminus of the central parallel region of the sheet. (**B**) View approximately perpendicular to (A). The tungstate ion is situated coincident with the axis of α-4. Figures produced by means of RIBBONS (*72*). Abbreviations for the amino acid residues are: A, Ala; C, Cys; D, Asp; E, Glu; F, Phe; G, Gly; H, His; I, Ile; K, Lys; L, Leu; M, Met; N, Asn; P, Pro; Q, Gln; R, Arg; S, Ser; T, Thr; V, Val; W, Trp; and Y, Tyr. WO_4, tungstate.

ods (Table 1). Sodium tungstate was used as a heavy atom derivative because we determined that the catalytic activity of PTP1B was effectively inhibited by low concentrations of tungstate (IC_{50} = 10 μM). All data were collected at beamline X8C (National Synchrotron Light Source at Brookhaven National Laboratory) on the "blue" charge-coupled device detector (*43*) and processed with the MADNES program (*44*). Ninety percent of the main chain and 75 percent of the side chain atoms were built into the initial electron density map with the graphics program O (*45*). After four cycles of model building, refinement, and phase combination, all residues from 5 to 282 were built into the electron density map. The NH_2-terminal four residues and the COOH-terminal 39 residues, which are outside the catalytic core, are not visible in the electron density map and are assumed to be disordered. The *R* factor, obtained from all data between 6 Å and 2.85 Å (99 percent complete) is 0.208, and the model possesses good stereochemistry (Table 1). Portions of the electron density maps are shown in Fig. 1.

The tungstate derivative data set was used to refine the PTP1B-tungstate ion complex with the refined native structure as the protein model. The tungstate ion binds to the protein at the catalytic site. The final *R* factor (0.197) was obtained from data between 6.0 and 2.85 Å (Table 1). Since tungstate binds tightly to and inhibits PTP1B, presumably functioning as an analog of phosphate, the structure of the tungstate-PTP1B complex provides information about the interactions between the enzyme and substrate.

Overall architecture. The 37-kD form of PTP1B is composed of a single domain, with the polypeptide chain organized into eight α helices and 12 β strands (Figs. 2 and 3). A 10-stranded mixed β sheet that adopts

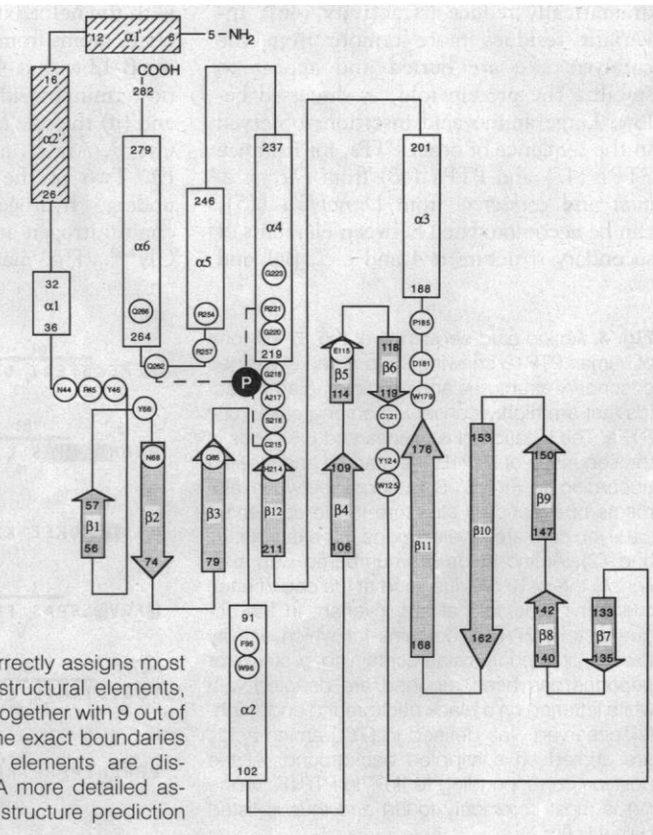

Fig. 3. Topology diagram showing the secondary structural elements of PTP1B. Hatched α helices α1′ and α2′ are amino-terminal to the conserved PTP catalytic core. The positions of invariant residues are indicated by open circles. The phosphate binding site is indicated by P. Dashed lines indicate side chain tungstate interactions. The secondary structure was assigned from amino acid phi psi angles and by H-bond requirements. The latter were assigned according to the method of Kabsch and Sander (*73*). A prediction of the secondary structure, derived from a multiple alignment of PTP sequences, compares well with the topology shown here (*74*). The prediction correctly assigns most of the essential secondary structural elements, namely, α helices α-2 to α-6 together with 9 out of the 12 β strands, although the exact boundaries of the secondary structure elements are displaced in some instances. A more detailed assessment of the secondary structure prediction will be published elsewhere.

a highly twisted conformation spans the entire length of the molecule. The final β strand, β-12, in the primary sequence, is located close to the center of the sheet within the parallel β strand region which has strand order β-3, β-12, β-4, and β-11. Antiparallel β strands flank the four central parallel β strands. The center of the sheet is buried by α helices with α-2 on one side and α-3 and α-4 on the other. Following α-4, the chain folds into α-5 and α-6, which, with α-3 and α-4, form a four-helix bundle. The COOH-terminus of the conserved catalytic domain corresponds to the COOH-terminus of α-6. A short α helix (α-1) found at the top of the β sheet close to β-1, marks the start of the conserved PTP domain. An antiparallel β sheet (β-5 and β-6) is located above the central β sheet. Finally, the non-conserved amino-terminal 30 residues fold into two α helices (α-1′ and α-2′) that wrap around the NH_2-terminus of α-6. To our knowledge the secondary structure topology (Fig. 3) represents a novel protein fold.

The catalytic cysteine (Cys^{215}) is situated on loop 15 connecting β-12 and α-4, at the COOH-terminus of the parallel β strand region of the sheet. Intervening loops connecting elements of secondary structure converge around this site. Most of the 27 invariant residues (Fig. 4) are found on these loops (Figs. 2 and 3). Individual mutations in many of the equivalent residues in the receptor-like PTP LAR (leukocyte common antigen-related protein) dramatically reduce its activity (*46*). Invariant residues more remote from the catalytic site are buried and appear to stabilize the protein fold, as discussed below. Large amino acid insertions observed in the sequence of other PTPs, for instance PTP1 (*47*) and PTPa (*48*) from *Dictyostelium* and *corkscrew* from *Drosophila* (*15*), can be accommodated between elements of secondary structure α-4 and α-5, β-1 and β-2, and β-2 and β-3, respectively.

Comparison of the native and tungstate-complexed structures show that they are virtually identical with equivalent atoms superimposing within a root-mean-square difference of 0.3 Å. As a result of tungstate binding, small motions of the side chains of Cys^{215}, Arg^{221}, and Gln^{262} occur in order to create interactions with the tungstate ion; differences in the refined coordinates are supported by the electron density maps.

Structure of the catalytic site. The catalytic site is located within a crevice on the molecular surface as identified by the location of the essential cysteine residue and the refined position of the inhibitory tungstate ion (Figs. 2 and 5). The base of the catalytic site is formed by residues from His^{214} to Arg^{221}, corresponding to the conserved motif characteristic of protein tyrosine phosphatases. This sequence forms the COOH-terminus of β-12, loop 15 connecting β-12 with α-4, and the NH_2-terminal turn of α-4 (Figs. 2 to 4) and contributes the essential catalytic cysteine and most of the residues required for phosphate binding. Loops surrounding the site that contain conserved amino acids are; *l*-1 (residues 37 to 55), *l*-4 (residues 86 to 90), *l*-13 (residues 177 to 187), and *l*-17 (residues 255 to 263). The small β sheet of β-5 and β-6 is located above the site (Figs. 2 and 4 to 6).

The phosphate binding site situated at the amino-terminus of α-4 is coincident with the helix axis. It is created by (i) main chain atoms from residues of the loop joining β-12 with α-4 (Ser^{216}–Gly^{218}) and amino-terminal residues of α-4 (Ile^{219}–Arg^{221}) and (ii) the side chains of invariant residues Cys^{215}, Arg^{221}, and Gln^{262} (Fig. 5, A and B). Two of the tungstate oxygen atoms undergo hydrogen-bonding to the main chain nitrogen atoms of Ser^{216}, Ile^{219}, and Gly^{220}. The main chain nitrogen atoms and the side chain of Arg^{221} encircle the tungstate ion, reminiscent of a rigid cradle structure (Fig. 5, A and B). In the absence of tungstate, the NH1 atom of Arg^{221} and the Sγ atom of Cys^{215} are 3.0 Å apart, suggestive of either an H bond or salt bridge (Fig. 5C). Localized protein conformational changes accompany tungstate binding (Fig. 5D). These involve a concerted motion of the side chains of Cys^{215} and Arg^{221} toward the tungstate ion by 2.0 and 1.5 Å, respectively. A salt bridge is created between a tungstate oxygen and the side chain of Arg^{221} while essentially preserving the interaction between Cys^{215} and Arg^{221} (the Sγ–NH1 distance becomes 3.5 Å). The position of Sγ of Cys^{215} is consistent with its role as a nucleophile in the catalytic mechanism. It forms equivalent contacts (2.7 Å) to two tungstate oxygen atoms. The Sγ–W distance is 3.1 Å, and the Sγ atom is approximately opposite the W–O1 and W–O2 bonds, one of which may correspond to the scissile bond of the phosphotyrosine substrate. The salt bridge between the side chains of Arg^{221} and Glu^{115} is partially disrupted as a result of tungstate binding; however, the main chain atoms of the phosphate binding site are unchanged (Fig. 5D). Two tungstate oxygen atoms (O1 and O2) are accessible to solvent and form H bonds to the amide side chain of Gln^{262} (Fig. 5, A and B).

The interactions of Arg^{221} with Cys^{215} and tungstate (as a phosphate analog) may explain its invariance in all active PTPs and dual specificity protein phosphatases. These observations are also consistent with the results of mutagenesis studies on Arg^{1528} of LAR (equivalent to Arg^{221} of PTP1B) which shows that replacement by any residue, including lysine, resulted in complete loss of enzyme activity (*5*).

Polar groups on neighboring conserved residues help to orient the phosphate bind-

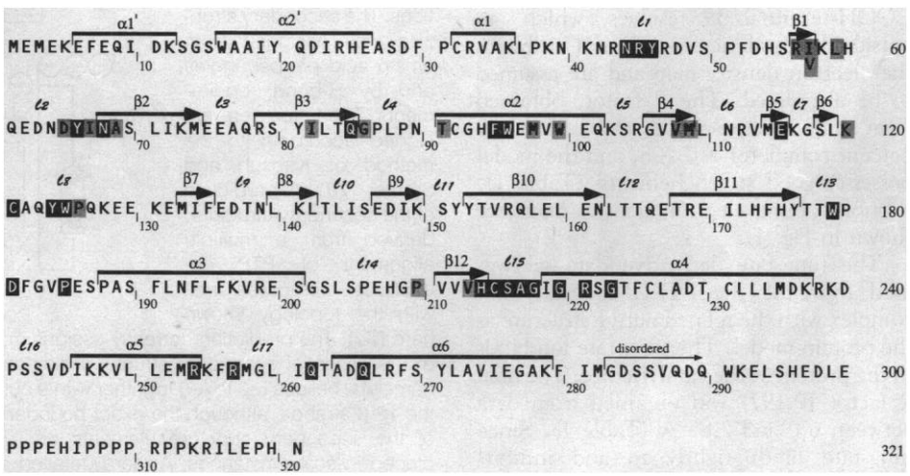

Fig. 4. Amino acid sequence of the 37-kD form of human PTP1B showing the position of defined secondary structures and highlighting amino acids that are highly conserved among eukaryotic PTPs. The location of α helices and β strands in the sequence of PTP1B are marked and labeled according to Fig. 3. Sequences between elements of secondary structure in the conserved catalytic core are labeled loops (for example, ℓ1 and ℓ2). Amino acids are numbered with subscripts every 10 residues and at the end of each line. Amino acids that are invariant in the sequences of 27 PTP domains for which activity toward phosphotyrosine-containing proteins or peptides has been reported are denoted with white lettering on a black background and "highly conserved" [as defined in (*76*)] amino acids are printed on a stippled background. At the position corresponding to Ile^{57} in PTP1B, valine (V) is most commonly found and thus is listed below Ile^{57}.

ing loop by forming H bonds to main chain carbonyl groups on the loop (Fig. 5B). These H bonds occur between (i) Cys^{215} and the side chain Nδ of His^{214}, (ii) Ser^{216} and the main chain N of Gly^{86}, (iii) Ala^{217} and the side chain NH1 of Arg^{257}, and (iv) Gly^{218} and the hydroxyl group of Ser^{222}. The latter H bond suggests why only Ser or Thr are found at position 222 within the PTP signature motif because the hydroxyl groups of both residues will form equivalent H bonds to the main chain of the phosphate binding loop. The buried environment of Arg^{257} is unusual. The side chain participates in a network of H bonds formed from a cluster of invariant residues, namely Asn^{44}, Tyr^{66}, and Asn^{68}. The position of Arg^{257} adjacent to the phosphate binding site probably contributes to the affinity for substrate as a result of an increase in the electrostatic potential at the catalytic site.

Four of the residues forming the phosphate binding site (Gly^{218} to Arg^{221}) occur within a GxGxxG sequence motif (Fig. 4), which is also found in a variety of phosphate binding proteins including dehydrogenases (*49*) and protein kinases (*50–53*). In PTP1B, the conformation of the motif more closely resembles but is distinct from its counterpart in the dehydrogenases (*54, 55*). The cAMP-dependent protein kinase crystal structures from mouse (*50, 51*) and porcine (*52*) show that in these enzymes the motif is situated within a structure termed the phosphate anchor, which consists of a hairpin loop connecting a pair of antiparallel β strands that form main chain nitrogen H bonds to the β and γ phosphates of adenosine triphosphate (ATP). In contrast, in PTP1B the first glycine occurs in loop 15 with the other residues as part of the α-4 helix. Main chain phi-psi angles for the glycine residues of the GxGxxG motif of PTP1B are within the allowed range for non-glycine amino acids. Gly^{218}, which is invariant in PTPs and dual specificity phosphatases, adopts a lefthanded conformation, producing a sharp turn in the structure. Like that in protein kinases, the glycine-rich motif of PTP1B facilitates close-packing of main chain atoms of the phosphate binding loop with phosphate oxygen atoms and neighboring protein residues. This is in agreement with the finding that replacing the first glycine of the motif with bulky side chains in the equivalent position in the PTP domain of LAR abolishes catalytic activity (*5*).

Role of the invariant residues His^{214} and Cys^{215}. Site-directed mutagenesis of the active site cysteine in a number of PTP domains including PTP1B (*6*), CD45 (*5*), and *Yersinia* PTP (*24*) causes complete loss

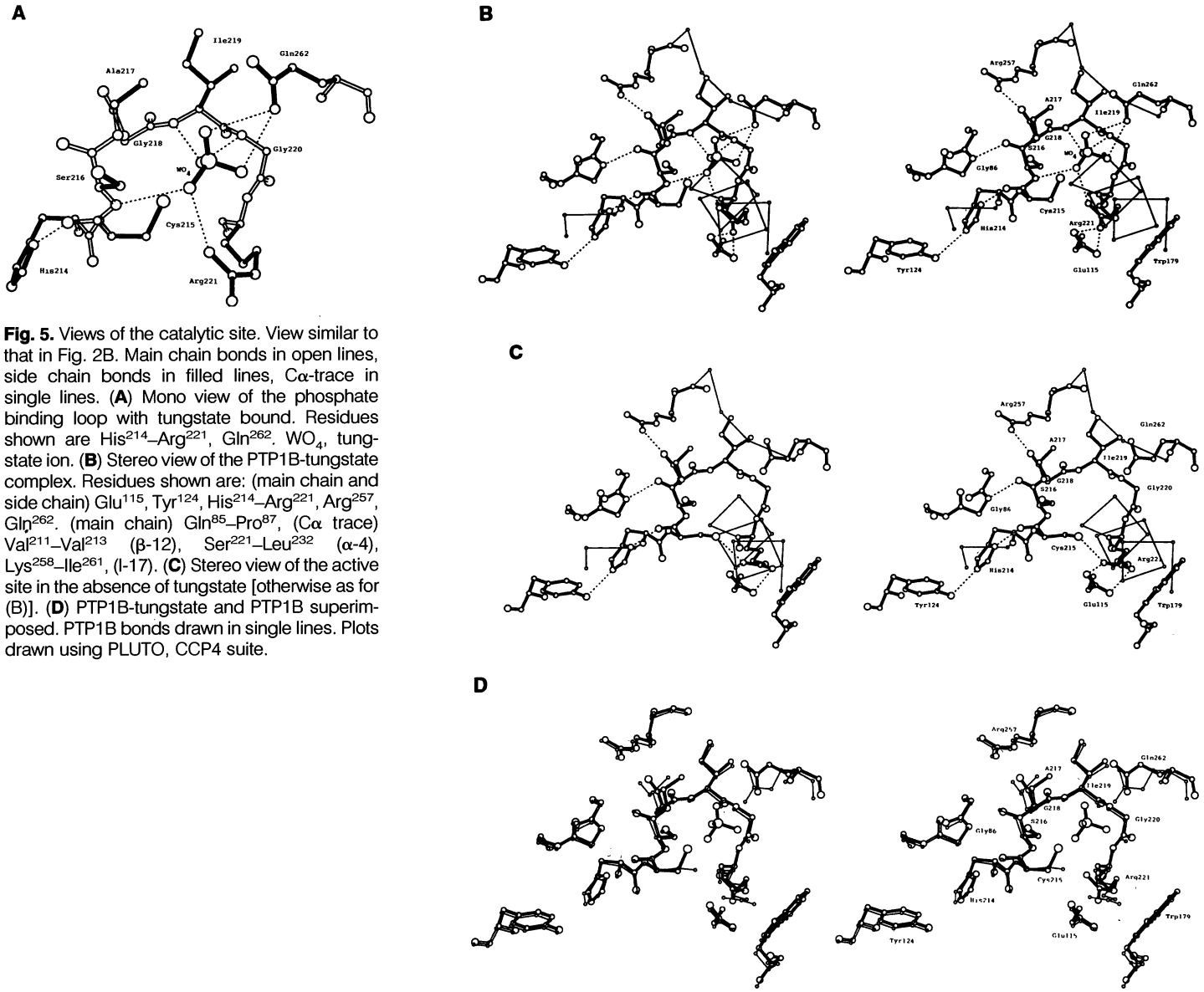

Fig. 5. Views of the catalytic site. View similar to that in Fig. 2B. Main chain bonds in open lines, side chain bonds in filled lines, Cα-trace in single lines. (**A**) Mono view of the phosphate binding loop with tungstate bound. Residues shown are His^{214}–Arg^{221}, Gln^{262}. WO_4, tungstate ion. (**B**) Stereo view of the PTP1B-tungstate complex. Residues shown are: (main chain and side chain) Glu^{115}, Tyr^{124}, His^{214}–Arg^{221}, Arg^{257}, Gln^{262}. (main chain) Gln^{85}–Pro^{87}, (Cα trace) Val^{211}–Val^{213} (β-12), Ser^{221}–Leu^{232} (α-4), Lys^{258}–Ile^{261}, (l-17). (**C**) Stereo view of the active site in the absence of tungstate [otherwise as for (B)]. (**D**) PTP1B-tungstate and PTP1B superimposed. PTP1B bonds drawn in single lines. Plots drawn using PLUTO, CCP4 suite.

of enzymatic activity. Studies of rat PTP1B show that the cysteine forms a thio-phosphate intermediate during the reaction mechanism (6). Serine is unable to substitute for cysteine, although substrate binding is not affected (56). The pK_a of the active site cysteine of *Yersinia* PTP is 4.7, indicating that the cysteine residue is a thiolate anion at physiological pH (57). The thiolate ion of Cys^{215} is stabilized by a salt bridge to Arg^{221} and by the helix dipole of α-4. The structure of the PTP1B-tungstate complex reveals the Sγ of Cys^{215} is ideally positioned to act as a nucleophile on a bound phosphotyrosine substrate (Fig. 5, A and B). The hydroxyl oxygen of the tyrosyl leaving group requires protonation after the formation of the thio-phosphate intermediate; however, the absence of potential proton donors within 8 Å suggests that an activated water molecule may fulfill this function.

The catalytic site cysteine is invariantly preceded by a histidine residue (His^{214} in PTP1B). Analysis of the structure reveals that the side chain of His^{214} forms one H bond through Nδ with the carbonyl oxygen of Cys^{215} and a second H bond through Nε with OH of the side chain of the invariant Tyr^{124} (Fig. 5). Since the side chain of His^{214} does not directly interact with either the phosphate ion or the side chain of Cys^{215}, a direct role for His^{214} in catalysis is unlikely. Its role appears to be a structural one in defining the conformation of Cys^{215} and the phosphate binding loop. In addition, the H bond to the carbonyl oxygen of Cys^{215} will augment the peptide dipole, increasing the partial positive charge on the main chain nitrogen of Ser^{216}, and thereby strengthen the H bond to tungstate (or phosphate) bound at the catalytic site. Our findings are in agreement with the results of site-directed mutagenesis experiments on the active site histidine of rat PTP1B (6) and LAR (His^{1521}) (5), showing that amino acid substitutions at this site reduced activity without completely abolishing it. A cluster of invariant hydrophobic residues surrounding Tyr^{124} and His^{214} consist of Phe^{95} and Trp^{96} of α-2 and Cys^{121} and Trp^{126} on *l*-8 (Figs. 2 and 3).

Implications for substrate binding. PTP1B acts specifically on proteins phosphorylated on tyrosine and is unable to dephosphorylate proteins phosphorylated on serine and threonine residues (32). A variety of phosphotyrosine proteins, phosphorylated by different protein tyrosine kinases, are substrates for PTP1B, suggesting that the overall structure of the substrate is not a strong determinant of selectivity, the primary determinant being the presence of phosphotyrosine in the context of a peptide.

We have used the structure of tungstate bound at the catalytic site of PTP1B in order to suggest a binding site for a phosphotyrosine residue. The sides of the cleft are formed from the side chains of Asp^{48}, Lys^{116}, Lys^{120}, and the invariant Tyr^{46}. These residues are candidates to form interactions with the tyrosine moiety of the substrate (Fig. 6A). The presence of lysines at the catalytic site of PTP1B is reminiscent of the arginine and lysine side chains, which form amino-aromatic interactions with the tyrosine moiety of a phosphotyrosine residue in the crystal structures of

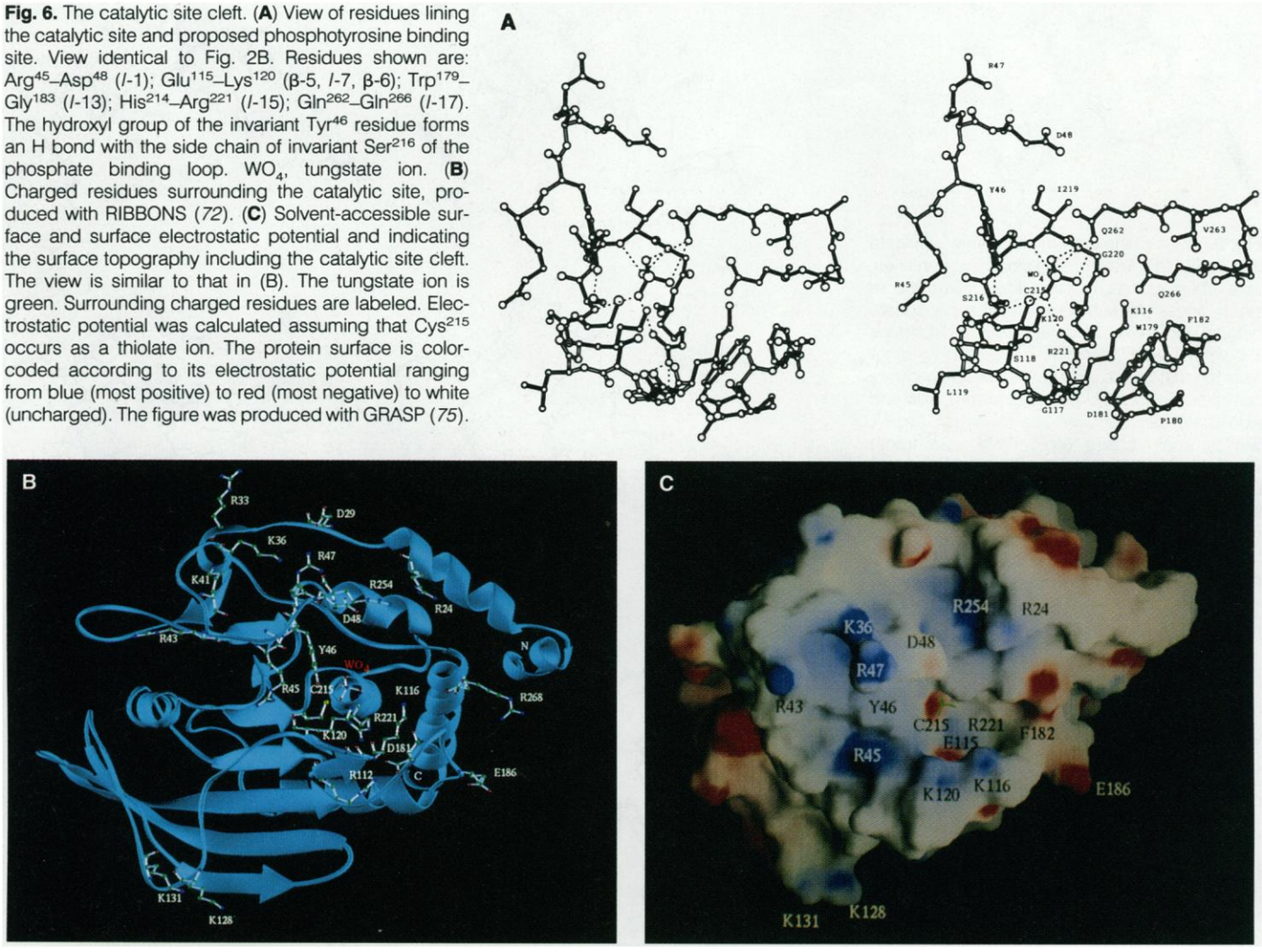

Fig. 6. The catalytic site cleft. (**A**) View of residues lining the catalytic site and proposed phosphotyrosine binding site. View identical to Fig. 2B. Residues shown are: Arg^{45}–Asp^{48} (*l*-1); Glu^{115}–Lys^{120} (β-5, *l*-7, β-6); Trp^{179}–Gly^{183} (*l*-13); His^{214}–Arg^{221} (*l*-15); Gln^{262}–Gln^{266} (*l*-17). The hydroxyl group of the invariant Tyr^{46} residue forms an H bond with the side chain of invariant Ser^{216} of the phosphate binding loop. WO_4, tungstate ion. (**B**) Charged residues surrounding the catalytic site, produced with RIBBONS (*72*). (**C**) Solvent-accessible surface and surface electrostatic potential and indicating the surface topography including the catalytic site cleft. The view is similar to that in (B). The tungstate ion is green. Surrounding charged residues are labeled. Electrostatic potential was calculated assuming that Cys^{215} occurs as a thiolate ion. The protein surface is color-coded according to its electrostatic potential ranging from blue (most positive) to red (most negative) to white (uncharged). The figure was produced with GRASP (*75*).

SH2 domains complexed to phosphotyrosine peptides (*58–60*).

Although phosphotyrosine alone is a relatively poor substrate, with a Michaelis constant (K_m) of 5 mM (*61*), the K_m toward a variety of phosphotyrosine peptides ranges from 0.2 to 60 μM. The enzyme displays a subtle preference for multiple acidic side chains within five amino acids amino-terminal to the phosphotyrosine residue (*61, 62*). Substitution of individual acidic residues with alanine within a given peptide substrate results in small changes in K_m of less than 10-fold (*61, 62*). A similar sequence preference for acidic residues is shown by HPTPβ (*63*).

Our crystal structure suggests that amino acids on the substrate surrounding the phosphotyrosine would be positioned to interact with residues on the surface of the phosphatase. The protein surface surrounding the catalytic cleft is relatively open and consists of a number of depressions and protrusions (Fig. 6, B and C). This might allow numerous modes of peptide binding, and perhaps explain the poor discrimination between phosphotyrosine proteins. The preference for acidic residues that are commonly found adjacent to physiological sites of tyrosine phosphorylation (*64*) and the inhibition of PTP1B activity by anionic molecules such as poly(Glu, Tyr) and heparin (*32*) may result from the high density of basic residues located on the enzyme surface surrounding the catalytic site (Fig. 6, B and C). Specificity for phosphotyrosine-containing peptides probably results from the depth of the cleft since the smaller phosphoserine and phosphothreonine side chains would not reach to the phosphate binding site. A similar mechanism was proposed to explain the specificity of SH2 domains toward phosphotyrosine peptides (*58*) and may represent a common biological method of distinguishing between phosphotyrosine and phosphoserine or phosphothreonine.

Relevance to other phosphatases. The PTP family of enzymes are structurally distinct from serine or threonine, acid, and alkaline phosphatases. As expected from the absence of sequence similarity, the overall architecture and structure of the catalytic site of PTP1B differs from both *E. coli* alkaline phosphatase (*65*) and rat prostatic acid phosphatase (*66*). The phosphate binding site of *E. coli* alkaline phosphatase is formed by two Zn^{2+} ions and the guanidinium group of an Arg residue and is adjacent to Ser^{102} which acts as a nucleophile in the catalytic reaction (*65*). On the basis of the conservation of amino acid sequence between the core catalytic domain of PTP1B and other members of the PTP family (mean identity of 40 percent), (Fig. 4), we expect that the structure of PTP1B reported above would be similar to that of other PTPs, including the receptor-like forms such as CD45. The structure reveals the mechanism of phosphate recognition and explains the role of invariant residues, His^{214}, Cys^{215}, and Arg^{221}, in the catalytic mechanism. Most of the structure required for phosphate binding and catalysis is provided by residues His^{214} to Arg^{221} present in the conserved signature motif that forms the base of the catalytic site cleft. Dual specificity phosphatases share only restricted sequence similarity with PTP1B that encompasses the catalytic site sequence Val^{213} to Gly^{223}. The absence of similarity elsewhere in the sequence suggests that the details of their three-dimensional structures may have diverged considerably whereas the crucial features required for phosphate recognition and catalysis are maintained. The concentration of residues participating in fundamental aspects of catalysis within a short sequence in protein tyrosine phosphatases suggests that, although it is important to conserve this sequence, the rest of the protein may change significantly in order to acquire characteristic specificities and functions.

REFERENCES AND NOTES

1. W. J. Fantl, D. E. Johnson, L. T. Williams, *Annu. Rev. Biochem.* **62**, 453 (1993).
2. H. Charbonneau and N. K. Tonks, *Annu. Rev. Cell Biol.* **8**, 463 (1992).
3. K. M. Walton and J. E. Dixon, *Annu. Rev. Biochem.* **62**, 101 (1993).
4. N. K. Tonks, Ed., *Seminars in Cell Biology* (Academic Press, London, 1993), vol. 4, pp. 373–453.
5. M. Streuli, N. X. Krueger, T. Thai, M. Tang, H. Saito, *EMBO J.* **9**, 2399 (1990).
6. K. L. Guan and J. E. Dixon, *J. Biol. Chem.* **266**, 17026 (1991).
7. D. A. Pot, T. A. Woodford, E. Remboutsika, R. S. Haun, J. E. Dixon, *ibid.*, p. 19688.
8. H. Cho *et al.*, *J. Am. Chem. Soc.* **114**, 7296 (1992).
9. S. M. Brady-Kalnay, A. J. Flint, N. K. Tonks, *J. Cell Biol.* **122**, 961 (1993).
10. S.-H. Shen, L. Bastien, B. I. Posner, P. Chretien, *Nature* **352**, 736 (1991).
11. T. Yi, J. L. Cleveland, J. N. Ihle, *Mol. Cell. Biol.* **12**, 836 (1992).
12. R. J. Matthews, D. B. Browne, E. Flores, M. L. Thomas, *ibid.*, p. 2396.
13. R. M. Freeman Jr., J. Plutzky, B. G. Neel, *Proc. Natl. Acad. Sci. U.S.A.* **89**, 11239 (1992).
14. G.-S. Feng, C.-C. Hui, T. Pawson, *Science* **259**, 1607 (1993).
15. L. A. Perkins, I. Larsen, N. Perrimon, *Cell* **70**, 225 (1992).
16. Q. Yang and N. K. Tonks, *Proc. Natl. Acad. Sci. U.S.A.* **88**, 5949 (1991).
17. M. Gu, J. D. York, I. Warshawsky, P. W. Majerus, *ibid.*, p. 5867.
18. M. Gu, I. Warshawsky, P. W. Majerus, *ibid.* **89**, 2980 (1992).
19. J. B. A. Millar and P. Russell, *Cell* **68**, 407 (1992).
20. H. Sun, C. H. Charles, L. F. Lau, N. K. Tonks, *ibid.* **75**, 487 (1993).
21. D. R. Alessi, C. Smythe, S. M. Keyse, *Oncogene* **8**, 2015 (1993).
22. M. Potts *et al.*, *J. Biol. Chem.* **268**, 7632 (1993).
23. K. L. Guan, S. S. Broyles, J. E. Dixon, *Nature* **350**, 359 (1991).
24. K. L. Guan and J. E. Dixon, *Science* **249**, 553 (1990).
25. L. D. Schultz *et al.*, *Cell* **73**, 1445 (1993).
26. H. W. Tsui, K. A. Siminovitch, L. deSouza, F. W. L. Tsui, *Nature Genet.* **4**, 124 (1993).
27. K. K. Wary *et al.*, *Cancer Res.* **53**, 1498 (1993).
28. J. T. Pingel and M. L. Thomas, *Cell* **58**, 1055 (1989).
29. G. A. Koretzky, J. Picus, M. L. Thomas, A. Weiss, *Nature* **346**, 66 (1990).
30. L. B. Justement, K. S. Campbell, N. C. Chien, J. C. Cambier, *Science* **252**, 1839 (1991).
31. N. K. Tonks, C. D. Diltz, E. H. Fischer, *J. Biol. Chem.* **263**, 6722 (1988).
32. ———, *ibid.*, p. 6731.
33. H. Charbonneau *et al.*, *Proc. Natl. Acad. Sci. U.S.A.* **86**, 5252 (1989).
34. K. L. Guan, R. S. Haun, S. J. Watson, R. L. Geahlen, J. E. Dixon, *ibid.* **87**, 1501 (1990).
35. J. Chernoff, A. R. Schievella, C. A. Jost, R. L. Erikson, B. G. Neel, *ibid.*, p. 2735.
36. S. Brown-Shimer, K. A. Johnson, J. B. Lawrence, C. Johnson, A. Bruskin, *ibid.*, p. 5148.
37. J. V. Frangioni, P. H. Beahm, V. Shifrin, C. A. Jost, B. G. Neel, *Cell* **68**, 545 (1992).
38. A. J. Flint, M. F. B. G. Gebbink, B. R. J. Franza, D. E. Hill, N. K. Tonks, *EMBO J.* **12**, 1937 (1993).
39. T. A. Woodford-Thomas, J. D. Rhodes, J. E. Dixon, *J. Cell Biol.* **117**, 401 (1992).
40. S. Brown-Shimer, K. A. Johnson, D. E. Hill, A. M. Bruskin, *Cancer Res.* **52**, 478 (1992).
41. K. A. Kenner, D. E. Hill, J. M. Olefsky, J. Kusari, *J. Biol. Chem.* **268**, 25455 (1993).
42. J. V. Frangioni, A. Oda, M. Smith, E. W. Salzman, B. G. Neel, *EMBO J.* **12**, 4843 (1993).
43. M. G. Strauss *et al.*, *Proc. Soc. Photo. Inst. Eng.* **1447**, 12 (1991).
44. A. Messerschmidt and J. W. Pflugrath, *J. Appl. Crystallogr.* **20**, 306 (1987).
45. T. A. Jones, J. Y. Zou, S. W. Cowan, M. Kjeldgaard, *Acta. Crystallogr.* **A47**, 110 (1991).
46. A. Y. M. Tsai, M. Itoh, M. Streuli, T. Thai, H. Saito, *J. Biol. Chem.* **266**, 10534 (1991).
47. P. K. Howard, B. M. Sefton, R. A. Firtel, *Cell* **71**, 637 (1992).
48. R. Ramalingam, D. R. Shaw, H. L. Ennis, *J. Biol. Chem.* **268**, 22680 (1993).
49. M. G. Rossmann, A. Lijas, C. Branden, L. Banaszak, *The Enzymes*, P. D. Boyers, Eds. (Academic Press, New York, 1975), vol. 11, p. 61.
50. D. R. Knighton *et al.*, *Science* **253**, 407 (1991).
51. D. R. Knighton *et al.*, *ibid.*, p. 414 (1991).
52. D. Bossemeyer, R. A. Engh, V. Kinzel, H. Ponstingl, R. Huber, *EMBO J.* **12**, 849 (1993).
53. H. L. De Bondt *et al.*, *Nature* **363**, 595 (1993).
54. Abad-Zapatero-C., J. P. Griffith, J. L. Sussman, M. G. Rossmann, *J. Mol. Biol.* **198**, 445 (1987).
55. F. C. Bernstein *et al.*, *ibid.* **112**, 535 (1977).
56. K. L. Milarski *et al.*, *ibid.* **268**, 23634 (1993).
57. Z.-Y. Zhang and J. E. Dixon, *Biochemistry* **32**, 9340 (1993).
58. G. Waksman, *et al.*, *Nature* **358**, 646 (1992).
59. G. Waksman, S. E. Shoelson, N. Pant, D. Cowburn, J. Kuriyan, *Cell* **72**, 779 (1993).
60. M. J. Eck, S. E. Shoelson, S. C. Harrison, *Nature* **362**, 87 (1993).
61. K. L. Hippen *et al.*, *Biochemistry* **32**, 12405 (1993).
62. Z.-Y. Zhang *et al.*, *Proc. Natl. Acad. Sci. U.S.A.* **90**, 4446 (1993).
63. H. Cho *et al.*, *Protein Sci.* **2**, 977 (1993).
64. R. B. Pearson and B. E. Kemp, *Methods Enzymol.* **200**, 62 (1991).
65. E. E. Kim and H. W. Wyckoff, *J. Mol. Biol.* **218**, 449 (1991).
66. G. Schneider, Y. Lindquist, P. Vihko, *EMBO J.* **12**, 2609 (1993).

66a. D. Barford, J. C. Keller, A. J. Flint, N. K. Tonks, a description of the conditions used to purify and crystallize the protein is in preparation.

67. W. Kabsch, *J. Appl. Crystallogr.* **21**, 916 (1988).
68. L. Weismann, *Computer Crystallogr.*, D. Sayre *et al.*, Eds. (Oxford Univ. Press, London, 1982), pp. 56–63.
69. W. Furey and S. Swaminathan, *Am. Cryst. Assoc. Mtg. Summ.* **18**, 73 (1990).
70. B. C. Wang, *Methods Enzymol.* **115**, 90 (1985).
71. A. T. Brunger, J. Kuriyan, M. Karplus, *Science* **235**, 458 (1987).
72. M. Carson and C. E. Bugg, *J. Mol. Graph.* **4**, 121 (1986).
73. W. Kabsch and C. Sander, *Biopolymers* **22**, 2577 (1983).

74. C. D. Livingston and G. J. Barton, *Int. J. Peptide Protein Res.*, in press.
75. A. Nicholls, R. Bharadwaj, B. Honig, *Biophys. J.* **64**, 166 (1991).
76. PTP domains were aligned by means of the multiple sequence alignment program PILEUP in the GCG software package of the Genetics Computer Group, Inc. (Madison, WI) using default parameters. The sequence identity between PTP1B and each of the other PTPs in their core catalytic domain, amino acids 31–280 of PTP1B, was calculated with the BESTFIT program. The mean overall identity to PTP1B is 40 percent. A measurement of the identity at each amino acid position in the multiple sequence alignment was obtained using the PLOTSIMILARITY program with the "identity" restriction applied. The identity score at each position is the average of the scores resulting from comparison of all possible pairs of sequences with an identical pair receiving a score of 1 and a non-identical pair receiving score 0. Identity scores of 1.0 reveal invariant amino acids and scores between 0.8 and 1.0 are defined here as "highly conserved." Each "highly conserved" amino acid is found in 24 or more of these aligned PTP domains. The data base accession numbers of the PTPs and their identities to PTP/B were hPTP1B (A33897, PIR, 100%), hTCPTP (P17706, SwissProt, 75%), DPTP61F (L11251, GenBank, 56%), hMEG1 (M68941, GenBank, 42%), hPTPH1 (P26045, SwissProt, 41%), hMEG2 (M83738, GenBank, 41%), hPTP-PEST (A45496, PIR, 38%), mPTP-PEP (M90388, GenBank, 39%), hSH-PTP1 (P29350, SwissProt, 40%), hSH-PTP2 (A46210, PIR, 40%), DdPTPa (L15420, GenBank, 47%), DdPTP1 (A44267, PIR, 35%), SpPYP1 (P27574, SwissProt, 34%), SpPYP2 (A45030, PIR, 37%), SpPYP3 (X69994, GenBank, 37%), ScPTP1 (P25044, SwissProt, 35%), hCD45-D1 (P08575, SwissProt, 38%), hPTPα-D1 (P18433, SwissProt, 38%), hLAR-D1 (Y00815, GenBank, 43%), hPTPδ-D1 (P23468, SwissProt, 41%), rPTPσ-D1 (L19180, GenBank, 43%), DLAR-D1 (M27700, GenBank, 38%), hPTPμ (P28827, SwissProt, 38%), mPTPκ-D1 (L10106, GenBank, 40%), hPTPζ-D1 (P23471, SwissProt, 39%), DPTP (P16620, SwissProt, 33%), hPTPβ (P23467, SwissProt, 42%).
77. Supported by the Robertson Research Fund (D.B.), NIH grant CA53840 (N.K.T.), and a Pew Scholar award in the Biomedical Sciences (N.K.T.), a Cancer Research Institute and F. M. Kirby Foundation Fellowship (A.J.F.). We thank J. W. Pflugrath for advice and discussions; X. Cheng, W. Furey, and S. Gamblin for discussions; B. Stillman and J. D. Watson for encouragement and support; E. Westbrook, R. Alkire, S. L. Ginell, L. J. Keefe, and J. Lazarz for assistance and for access to beamline X8C at the National Synchrotron Light Source, Brookhaven National Laboratory; G. J. Barton for access to unpublished data; and H. Charbonneau, J. Horton, J. W. Pflugrath, and B. Stillman for comments on the manuscript. The atomic coordinates have been submitted to the Brookhaven protein data base.

25 January 1994; accepted 24 February 1994

The 2.9 Å Crystal Structure of *T. thermophilus* Seryl-tRNA Synthetase Complexed with $tRNA^{Ser}$

Valérie Biou, Anna Yaremchuk, Michael Tukalo, Stephen Cusack*

The crystal structure of *Thermus thermophilus* seryl-transfer RNA synthetase, a class 2 aminoacyl-tRNA synthetase, complexed with a single $tRNA^{Ser}$ molecule was solved at 2.9 Å resolution. The structure revealed how insertion of conserved base G20b from the D loop into the core of the tRNA determines the orientation of the long variable arm, which is a characteristic feature of most serine specific tRNAs. On tRNA binding, the antiparallel coiled-coil domain of one subunit of the synthetase makes contacts with the variable arm and TΨC loop of the tRNA and directs the acceptor stem of the tRNA into the active site of the other subunit. Specificity depends principally on recognition of the shape of $tRNA^{Ser}$ through backbone contacts and secondarily on sequence specific interactions.

Aminoacyl-tRNA synthetases perform an essential step in assuring the accuracy of protein synthesis by specifically ligating amino acids to their cognate tRNA isoacceptors. This occurs in a two-step reaction in which the amino acid is first activated by adenosine triphosphate (ATP) to form the aminoacyl-adenylate intermediate and is subsequently transferred to the 3′ terminal ribose of the tRNA. Considerable progress has been made in understanding the structural basis of specificity by application of sequence analyses, site-directed mutagenesis of tRNAs and synthetases, chemical probing of synthetase-tRNA complexes and x-ray crystallography. On the basis of short conserved primary sequence motifs the 20 aminoacyl-tRNA synthetases have been partitioned into two classes, each containing 10 members (*1*). This has largely resolved the problem of the apparent wide diversity of synthetase primary and quarternary structures. From the known crystal structures of five synthetases it is now clear that this partition corresponds in structural terms to the existence of a Rossmann fold in the catalytic domain of class 1 synthetase—exemplified by the crystal structures of the tyrosyl- (*2*), methionyl- (*3*) and glutaminyl- (*4*) tRNA synthetases) and an antiparallel fold in the catalytic domain of class 2 synthetases as seen in the crystal structures of the seryl- (*5*) and aspartyl- (*6*) tRNA synthetases. Apart from the catalytic domain, aminoacyl-tRNA synthetases contain other domains, often as COOH- or NH_2-terminal extensions. These putative tRNA binding domains show more idiosyncratic sequence and structural variability than the catalytic domains although, within subclasses, such domains can be homologous (*7*).

Of particular interest are the determinants of the specific recognition between a synthetase and its cognate tRNAs. For many systems, tRNA identity elements have been located (*8*); that is, nucleotides that are crucial to the specific recognition and whose transplantation into other tRNAs can change their amino acid identity. In most cases, the identity elements include some or all of the anticodon nucleotides (the exceptions being the tRNAs for serine, alanine, and leucine in *Escherichia coli*). However other nucleotides, often in the acceptor stem, can be important for identity as well. The two published crystal structures of synthetase-tRNA complexes, the glutamine system (*4*, *9*) from *E. coli* (class 1) and the aspartic acid system (*6*, *10*) from yeast (class 2) reveal examples of specific anticodon recognition. In both cases an additional domain is responsible, but the fold of this domain and the distortion induced in the anticodon stem and loop of the tRNA are different (*9*, *10*). Similarly, the mode of entry of the 3′ end of the tRNA into the active site is not the same in the two systems (*6*) with the net result, presumably, being the correct positioning of the 2′ OH (class 1) or 3′ OH (class 2) of the terminal ribose for receiving the amino acid (*1*).

In view of the idiosyncracies of each synthetase system, it is necessary to obtain detailed structural information about other tRNA-synthetase complexes in order to identify common and distinct features. The seryl-tRNA synthetase, an α_2 dimeric class 2 synthetase, warrants inspection for several reasons. First, because of the variety of serine codons (from two distinct codon groups), it is not surprising that the anticodon is not recognized by the synthetase (*11–14*); this is consistent with the existence of a serine amber suppressor tRNA and the opal suppressor $tRNA^{SelCys}$, both of which are specifically charged by seryl-tRNA synthetase. Second, most $tRNA^{Ser}$ moieties are peculiar in having a long variable arm of up to 20 nucleotides, a feature shared in prokaryotic systems only by $tRNA^{Leu}$ and $tRNA^{Tyr}$. To our knowledge,

The authors are at the European Molecular Biology Laboratory, Grenoble Outstation. c/o ILL, 156X, 38042 Grenoble Cedex, France. A. Yaremchuk and M. Tukalo are on leave from the Institute of Molecular Biology and Genetics, Kiev, Ukraine.

*To whom correspondence should be addressed.